Numerical investigation of cavitation generated by an ultrasonic dental scaler tip vibrating in a compressible liquid

Manmi, Kawa; Wu, W. B. ; Vyas, Nina; Smith, Warren; Wang, Qian; Walmsley, Damian

DOI:
10.1016/j.ultsonch.2020.104963

License:
Other (please provide link to licence statement

Document Version
Publisher's PDF, also known as Version of record

Citation for published version (Harvard):
Manmi, K, Wu, WB, Vyas, N, Smith, W, Wang, Q & Walmsley, D 2020, 'Numerical investigation of cavitation generated by an ultrasonic dental scaler tip vibrating in a compressible liquid', *Ultrasonics Sonochemistry*, vol. 63, 104963. https://doi.org/10.1016/j.ultsonch.2020.104963

Ultrasonics - Sonochemistry 63 (2020) 104963

Contents lists available at ScienceDirect

Ultrasonics - Sonochemistry

journal homepage: www.elsevier.com/locate/ultson

Numerical investigation of cavitation generated by an ultrasonic dental scaler tip vibrating in a compressible liquid

K.M.A. Manmi[a,b], W.B. Wu[c], N. Vyas[d], W.R. Smith[a], Q.X. Wang[a,*], A.D. Walmsley[d]

[a] School of Mathematics, College of Engineering and Physical Sciences, University of Birmingham, Birmingham, United Kingdom
[b] Department of Mathematics, College of Science, Salahaddin University-Erbil, Kurdistan Region, Iraq
[c] College of Engineering, Peking University, Beijing 100871, China
[d] School of Dentistry, College of Medical and Dental Sciences, University of Birmingham, Birmingham, United Kingdom

ARTICLE INFO

Keywords:
Vibro-acoustics
Finite element method
Cavitation
Dental implant
Ultrasonic scaler tip

ABSTRACT

Bacterial biofilm accumulation around dental implants is a significant problem leading to peri-implant diseases and implant failure. Cavitation occurring in the cooling water around ultrasonic scaler tips can be used as a novel solution to remove debris without any surface damage. However, current clinically available instruments provide insufficient cavitation around the activated tip surface. To solve this problem a critical understanding of the vibro-acoustic behaviour of the scaler tip and the associated cavitation dynamics is necessary. In this research, we carried out a numerical study for an ultrasound dental scaler with a curved shape tip vibrating in water, using ABAQUS based on the finite element method. We simulated the three-dimensional, nonlinear and transient interaction between the vibration and deformation of the scaler tip, the water flow around the scaler and the cavitation formation and dynamics. The numerical model was well validated with the experiments and there was excellent agreement for displacement at the free end of the scaler. A systematic parametric study has been carried out for the cavitation volume around the scaler tip in terms of the frequency, amplitude and power of the tip vibration. The numerical results indicate that the amount of cavitation around the scaler tip increases with the frequency and amplitude of the vibration. However, if the frequency is far from the natural frequency, the cavitation volume around the free end decreases due to reduced free end vibration amplitude.

1. Introduction

Dental plaque accumulates on teeth and dental implants and requires regular removal to prevent disease. Plaque can mineralise, requiring clinical intervention for removal, using instruments such as ultrasonic scalers. They have a rigid metal tip which vibrates at resonant frequencies between 25 and 40 kHz [1] and are lightly scraped along teeth in order to clean bacterial biofilm and other contaminated deposits from on and around the teeth surfaces [2,3]. However, the tip cannot be used effectively for cleaning biofilm from dental implants, as the metal (titanium implant) to metal (stainless steel tip) contact causes damage. Other methods of implant cleaning, such as rotating brushes or titanium tips have not been shown to be effective [4,5]. Therefore, research is being undertaken into novel methods of biofilm disruption. One method is using cavitation occurring in the cooling water around ultrasonic scaler tips to allow a non-touch approach.

Cavitation is a phenomenon in which rapid changes of pressure in a liquid lead to the formation of small vapor-filled cavities, in places where the pressure is relatively low [6,7]. Cavitation phenomena such as rapid micro-jet impingement, shock waves and microstreamers can lead to particle removal and erosion on solid surfaces [8,9]. Ultrasonic cavitation cleaning has been applied for in a range of industries, for example to remove marine biofouling or food contamination [10–12] or to remove biofilms [13–16]. Previous studies have confirmed that the cavitation occurs around dental scaler tips and aids the cleaning process [17–19], however it is not sufficient to enable rapid cleaning for clinical applications [18].

Increasing the cavitation generated by an oscillating scaler tip will lead to novel clinical approaches to the cleaning process. Numerical modelling of the tip will provide an insight into how cavitation may be increased by changing various parameters such as frequency. The data from numerical modelling can then inform decisions about how to optimize the instrument in experimental investigations. We will carry out a numerical study for an ultrasonic dental scaler with a curved tip vibrating in water considering cavitation generation in the liquid. The fluid flow is modelled by the linear potential flow theory in terms of

* Corresponding author.
E-mail address: q.x.wang@bham.ac.uk (Q.X. Wang).

https://doi.org/10.1016/j.ultsonch.2020.104963
Received 29 August 2019; Received in revised form 8 January 2020; Accepted 8 January 2020
Available online 09 January 2020

pressure, the deformation of the scaler tip is modelled by isotropic linear elastic theory, and their interaction is modelled through the kinetic and dynamic boundary conditions at their interface. The computations are carried out using ABAQUS based on the finite element method. The cavitation generation is associated with the evaporation of liquidized gases subject to low pressure. The detailed micro-processes of cavitation generation still remain elusive [20]. The pressure cutoff model has been used in the acoustic finite element transient analysis [21–25]. Wardlaw and Luton [24] noticed that the pressure cutoff has little impact on the solution as long as it is positive and small compared to 1 bar [23,24]. The Blake pressure threshold is given in terms of the surface tension, temperature and mass in a bubble [25]. The mass in bubbles is only available after detailed modelling of the evaporation and condensation across the bubble surfaces.

The physical, mathematical and numerical models are described in §2. In §3, the numerical model is validated by comparing with experimental data for the time history of the displacement at the free end of the scaler. In §4, a systematic parametric study has been carried out for the cavitation volume around the scaler tip in terms of the frequency, amplitude and power of the tip vibration. The numerical results indicate that the amount of cavitation around the scaler tip increases with the frequency and amplitude of the vibration.

2. Interaction modelling of the vibrating scaler tip

A commercially available ultrasonic scaler tip was modelled (Tip 10P, Acteon Group, USA), as the scaler tip is an irregular shape, a numerical model was needed to simulate the three-dimensional, nonlinear and transient interaction between the vibrating tip and the surrounding fluid considering the cavitation formation and dynamics. Assume that the scaler tip is completely submerged in a cuboid tank of water (Fig. 1c). The vibrations at the scaler tip produce pressure disturbances in the surrounding water. As a physical system the motion of the scaler tip (structure) and water (fluid) interact strongly with each other. Therefore, fluid-structure interactions (FSI) should be considered in the calculations of the pressure and vibration displacement. The analytical solution for the FSI problems exists for only a few simple geometric shapes. Generally, the numerical procedure of the FSI problem is classified into two approaches. A monolithic approach in which both fluid and solid are treated as one unified system, and a partitioned approach in which the fluid and solid are treated as two different systems coupled through the interface. A partitioned approach was chosen here to resolve the coupled problem. The partitioned approach allows existing fluid and structure solvers to be used with minimal code modifications. The coupling between the fluid and structure takes place at the fluid–structure boundary (Fig. 2). The boundary should be identical for both fluid and structure domains to accommodate the fluid–structure interaction [26–28].

In this model, the scaler tip is truncated near to the end which is fixed to the handpiece (Fig. 1a). The geometries of the truncated scaler tip and fluid domain in cuboid shape were displayed in Fig. 1b & c. The height and length of the scaler tip is 20 mm with varying circular cross section. The cross-section-radius at the truncated end of the scaler tip is 1.01 mm, and decreases slightly towards to the straight part and then decreases rapidly towards to the free end with a final value of 0.01 mm (Fig. 1b).

The dimension of the fluid domain was chosen as 40 mm (length) × 20 mm (width) × 40 mm (height), which are relatively large in comparison with the scaler tip dimensions to avoid nonphysical reflections of waves from the far boundary of the computational domain.

The Cartesian coordinate system *oxyz* is adopted so that length, height and width of the fluid domain (cuboid) are parallel to the *x*, *y* and *z*-axis respectively and the origin *o* at its centre. The scaler tip is positioned at the centre of the cuboid in such a way that the free and truncated ends are equally far from left and right cuboid boundaries respectively and the straight part is along the *x*-axis (see Fig. 2).

2.1. Acoustic modelling and cavitation

Assume that the water flow is inviscid and compressible and can be described by the linear potential flow theory. The momentum equation of the fluid experiencing velocity-dependent momentum losses can be expressed as [22,29–32],

$$\nabla p + \gamma \frac{\partial \mathbf{u}_f}{\partial t} + \rho_f \frac{\partial^2 \mathbf{u}_f}{\partial t^2} = 0, \tag{1}$$

with the constitutive linear behavior of the fluid,

$$\frac{\partial p}{\partial t} = -K_f \frac{\partial (\nabla \cdot \mathbf{u}_f)}{\partial t}, \tag{2}$$

where the ∇ represents the nabla operator, γ is the volumetric drag (force per unit volume per velocity), p is the pressure in the fluid. $\mathbf{x}$, $\mathbf{u}_f$ and ρ_f are the spatial position, directional displacement and the density of the fluid, respectively. K_f represents the bulk modulus of the fluid which is a constant for the problem under consideration.

To obtain the partial differential equation used in direct integration transient analysis in terms of pressure, Eq. (1) is divided by ρ_f and the divergence is evaluated with respect to $\mathbf{x}$. The result is then combined with the time derivatives of Eq. (2) with the derivative of γ/ρ_f neglected. We obtain

$$\frac{1}{K_f}\frac{\partial^2 p}{\partial t^2} + \frac{\gamma}{\rho_f K_f}\frac{\partial p}{\partial t} - \nabla \cdot \left(\frac{1}{\rho_f}\nabla p\right) = 0. \tag{3}$$

This equation would be equivalent with the linear wave equation, in the case that the volumetric drag and nonlinear terms were neglected in (1),

Introducing an arbitrary variation field δp, and integrating Eq. (3)

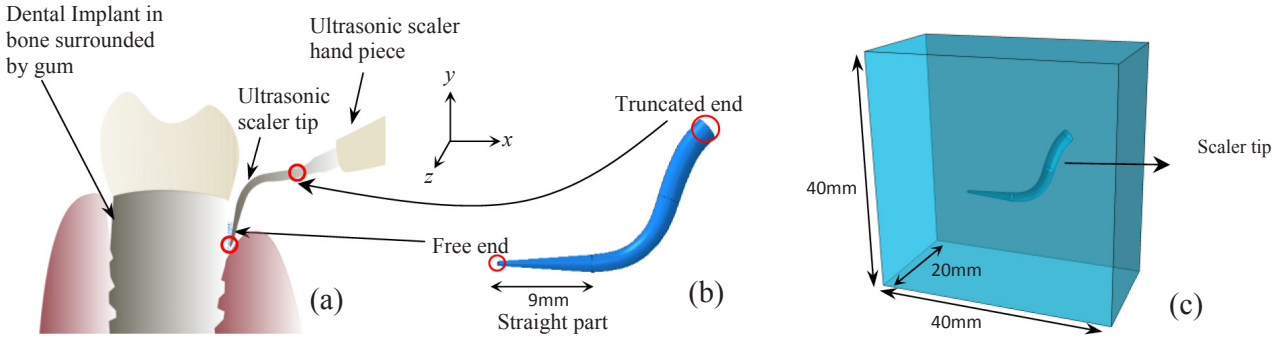

Fig. 1. (a) Schematic problem description of ultrasonic scaler tip and dental implant, (b) extracted digital geometry of the structure (truncated 10P tip) and (c) the cuboid computational fluid domain shape with the dimensions 40 mm × 40 mm × 20 mm.

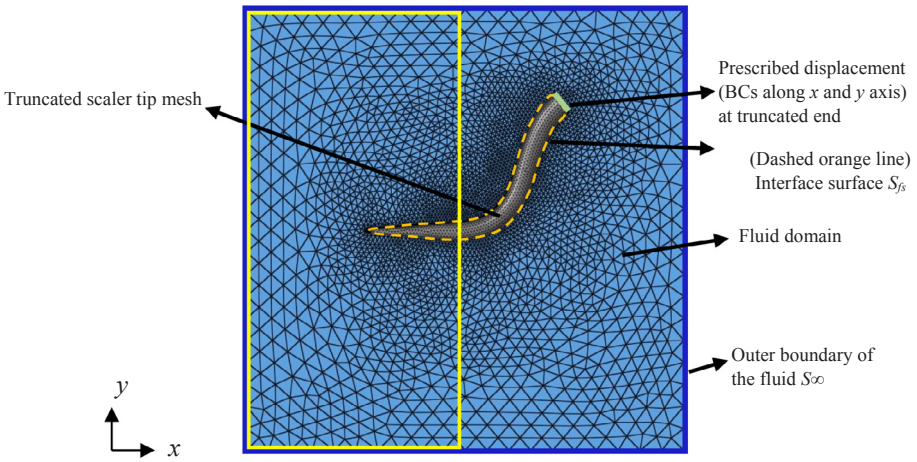

Fig. 2. Cross section of the tetrahedral mesh of the geometries at the plane *oxy* with labels indicating the position of the displacement boundary condition at the truncated end (green line), the interface surface (dashed orange line) and the outer boundary of the cuboid (Blue line). (For interpretation of the references to color in this figure legend, the reader is referred to the web version of this article.)

over the whole fluid field V_f, an equivalent weak form for the equation of motion can be obtained

$$\int_{V_f}\left(\frac{1}{K_f}\frac{\partial^2 p}{\partial t^2}+\frac{\gamma}{\rho_f K_f}\frac{\partial p}{\partial t}-\nabla\cdot\left(\frac{1}{\rho_f}\nabla p\right)\right)\delta p\, dV=0. \tag{4}$$

Green's theorem allows this to be rewritten as,

$$\int_{V_f}\left(\left(\frac{1}{K_f}\frac{\partial^2 p}{\partial t^2}+\frac{\gamma}{\rho_f K_f}\frac{\partial p}{\partial t}\right)\delta p+\nabla\delta p\cdot\frac{\nabla p}{\rho_f}\right)dV+\int_{S_{fs}+S_\infty} T(\mathbf{x})\,\delta p\, dS=0, \tag{5}$$

where S_{fs} and S_∞ are the structure and the far field boundary surface of the fluid domain, respectively, and

$$T(\mathbf{x})=-\frac{\mathbf{n}\cdot\nabla p}{\rho_f}, \tag{6}$$

where $\mathbf{n}$ represents the inward normal to the fluid at the boundary.

Two boundary conditions should be prescribed on the fluid surfaces S_{fs} and S_∞ through the last term of Eq. (5). Firstly, to consider the fluid as an unbounded domain the outgoing waves should be absorbed, or the wave reflection minimized on S_∞. This can be achieved here by considering non-reflection boundary condition through the use of impedance boundary conditions with the proper choice of impedance coefficients

$$T(\mathbf{x})=-\left(\frac{1}{c_1}\frac{\partial p}{\partial t}+\frac{1}{a_1}p\right), \tag{7}$$

in which

$$\frac{1}{c_1}=\frac{L}{\sqrt{\rho_f K_f}},\qquad \frac{1}{a_1}=L\left[\frac{\beta}{\rho_f}+\frac{\gamma}{2\rho_f\sqrt{\rho_f K_f}}\right], \tag{8}$$

where L is a geometric factor related to the metric factors of the curvilinear coordinate system used on the boundary and β is a spreading loss term. In the current model, we have chosen the planar geometry (cuboid) so $L=1$ and $\beta=0$. More details can be found in [22,30,33].

Secondly, the fluid-structural interaction boundary condition must be applied by equating the normal components of the displacements of the fluid and structure (scaler tip)

$$\mathbf{n}\cdot\mathbf{u}_s=\mathbf{n}\cdot\mathbf{u}_f, \tag{9}$$

Thus from (1) and (6) we get

$$T(\mathbf{x})=\mathbf{n}\cdot\left(\frac{\partial^2\mathbf{u}_s}{\partial t^2}+\frac{\gamma}{\rho_f}\frac{\partial\mathbf{u}_s}{\partial t}\right), \tag{10}$$

where $\mathbf{u}_s$ is the displacement of the structure. The volumetric drag is considered to be zero in this study as it is small compared with the fluid inertia.

We assume that cavitation happens instantaneously when the pressure in the liquid is smaller than a threshold p_c, which is taken to be 0 for calculation in this work. After considering cavitation, the pressure p in the liquid takes

$$p=\max\{p,\ p_c\}. \tag{11}$$

2.2. Structure modelling

Suppose the structure (scaler tips) with volume V and boundary surface S obeys the isotropic linear elastic theory and is under the action of the external forces: body force $\mathbf{b}$ and surface force $\mathbf{t}$. Its displacement $\mathbf{u}_s$ governed by the linear momentum equation is

$$\nabla\cdot\boldsymbol{\sigma}_s+\rho_s\mathbf{b}=\rho_s\frac{\partial^2\mathbf{u}_s}{\partial t^2}, \tag{12}$$

where $\boldsymbol{\sigma}_s$ and ρ_s are the Cauchy stress tensor and density of a point in the structure, respectively.

The dynamic boundary condition at the interface of the structure and fluid is the continuous normal stress

$$\mathbf{n}\cdot\boldsymbol{\sigma}_s=-\mathbf{n}\cdot\boldsymbol{\sigma}_f, \tag{13}$$

where $\mathbf{n}$ is the outward normal to the structure.

Integrate the dot product of $\delta\mathbf{u}_s$ with Eq. (12) over V and using Gauss theorem with the gradient identity for the first term in the left side. Moreover, neglecting all loading terms (such as damping, gravity) except the fluid pressure and surface traction gives us

$$\int_V \delta\varepsilon:\boldsymbol{\sigma}_s\, dV+\int_V \rho_s\,\delta\mathbf{u}_s\cdot\ddot{\mathbf{u}}_s dV+\int_{S_{fs}} p\delta\mathbf{u}_s\cdot n\, dS-\int_{S_t}\delta\mathbf{u}_s\cdot\mathbf{t}\, dS=0, \tag{14}$$

where $\delta\mathbf{u}_s$ is the variational displacement field, $\delta\varepsilon$is the strain variation of $\delta\mathbf{u}_s$, p is the pressure acting on the fluid-structural interface (S_{fs}) and $\mathbf{t}$ is the surface traction applied to the structure surface (S_t).

Numerically, a coupling element is placed along the boundary which has a vibration Degree of Freedom (DoF) on the side that couples the structure and a pressure DoF that couples the fluid. Accordingly, s_t denotes the surface traction on the structure side and s_{fs} denotes the fluid pressure on the fluid side.

2.3. Discretization finite element equations

The discretization of Eqs. (5) and (14) yields the mass matrix of the fluid along with the stiffness matrix. This is achieved by introducing interpolation functions: in the fluid $p=H^A p^A$, $A=1, 2, \ldots$ up to the number of pressure nodes and p^A is the pressure at the node A; in the

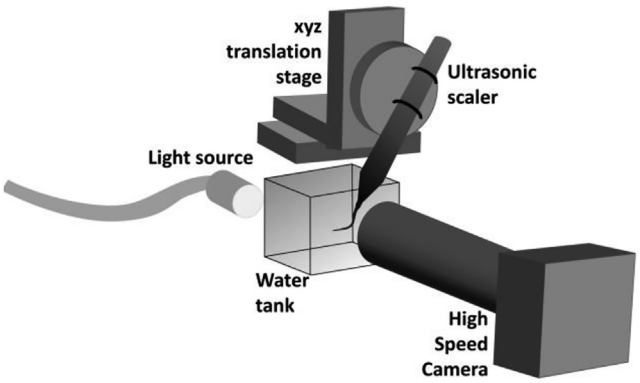

Fig. 3. Schematic of the experimental setup for high-speed imaging to measure the displacement oscillations at the free and truncated ends.

structure $\mathbf{u}_s = \mathrm{N}^B u_s^B$; $B = 1, 2, \ldots$ up to the number of displacement degrees of freedom, u_s^B is the displacement component at the node B. In the above H and $\mathbf{N}$ are the interpolation functions and the following equations assumed that summation is over the superscripts that refer to the degree of freedom in the discretized model.

Using Galerkin method and the Petrov-Galerkin substitution, the discretized coupled variational equation is obtained by adding Eqs. (5) and (14) to give

$$-\delta\hat{p}^A\{M_f^{AQ}\ddot{p}^Q + (K_f^{AQ} + K_{f\infty}^{AQ})p^Q - S_{fs}^{AM}\ddot{u}_s^M\} + \delta u_s^B\{I^B + M^{BM}\ddot{u}_s^M + [S_{fs}^{QB}]^T p^Q - p^B\} = 0, \quad (15)$$

where the superscripts A and Q refer to pressure degrees of freedom in the fluid, and B and M refer to displacement degrees of freedom in the structure. The bracketed terms are integral expressions of the interpolation functions for the structural and fluid domains [22,31].

2.4. Mesh, material properties and time steps

Mesh quality is an important factor in determining the stability and accuracy of computations. To describe accurately the propagation of the acoustic wave, the element size should be at least one order smaller than the acoustic wavelength $\lambda = c/f$, where c is the speed of acoustic wave and f is the frequency of the wave. For the calculations considered in this paper: $c = 1463$ m/s and $f = 20$–56 kHz, the range of λ is thus in the range of 26–73 mm. As such, we chose the element sizes of the mesh of the fluid domain to be in the range of 0.02–0.2 mm.

An unstructured mesh with tetrahedral elements is carried out for the fluid domain based on two considerations. Firstly, the unstructured mesh is body fitted, which is crucial for simulating the fluid–structure interaction. Secondly, a non-uniform mesh density is necessary to save CPU time and this is conveniently achieved by using an unstructured mesh. In this study the mesh element sizes in the fluid domain increased gradually from being 0.02 mm at the scaler surface to 0.2 mm at the external boundaries of the computational domain (Fig. 2), while the element size in the structure mesh was nearly uniform and about 0.06 mm.

Meshing was performed via the HyperMesh mesh generation software (version 2017.2, Altair Engineering Inc.), with their maximum skewness 0.96, maximum aspect ratio ≤ 3 for 99.99% of element and the rest ≤ 5, and minimum tetra collapse is 0.11 and for 93% of the elements between 0.2 and 0.5. The total fluid and structure elements were about 26 and 2 million, respectively. The computation was carried out with a high performance computing facility with 20 processors and the run time was approximately 50 hours. The volumes of cavitation at each time step was calculated in the whole fluid domain and around the straight part as shown in the yellow frame in Fig. 2.

The time integration was carried out using the explicit central-difference. The time step Δt, is given as the time needed for acoustic wave to pass across the smallest element in the mesh, which is known as Courant-Friedrich-Lewy (CFL) condition for the stability,

$$\Delta t \approx \frac{L_{\min}}{c}, \quad (16)$$

where $L_{\min}$ is the smallest element size in the model.

The fluid (water) properties are given as the bulk modulus of $K = \rho c^2 = 2140$ MPa, density $\rho = 10^3$ kg/m^3, c is speed of sound and the hydrostatic pressure 0.1 MPa. The scaler tip is made of stainless steel with the following material properties: Young's modulus $= 210 \times 10^3$ MPa, Poisson's ratio $= 0.3$, and the density 7.85×10^3 kg/m^3 [34].

3. Numerical validation

To evaluate the numerical modelling, we will compare the numerical results with the experimental data.

3.1. Tip vibration measurements using high-speed imaging

In the experiments, high-speed imaging and image analysis was used to calculate the vibration displacement of the ultrasonic scaler tip. A P5 Newtron XS scaler (Satelec, Acteon, France) operating at ~29 kHz was used in conjunction with Tip 10P. The tip was immersed in reverse osmosis water in a tank with dimensions 750 (length) × 52 (width) × 50 (height) mm. The scaler position was fixed by attaching it to a XYZ translation stage (PT3, Thorlabs Inc, NJ, USA) and a high-precision rotation mount (PRO1/M, Thorlabs Inc, NJ, USA). The axial rotation of the scaler tip was also maintained during each experiment (Fig. 3).

The scaler was illuminated using an LED cold light source (Hayashi HDF7010, Japan) in bright field mode. The deformation of the scaler tip was imaged using a high-speed camera (Photron Fastcam mini AX200) at 900,000 frames per second (fps). The camera was attached to a long distance microscope zoom lens (12x zoom lens system, Navitar, USA) with a 2x adaptor at a magnification of x7, giving a resolution of 1.429 μm/pixel (Fig. 3). Imaging was done at two points along the tip – the free end and the truncated end. The locations of imaging are indicated in Fig. 1a.

The tip displacement was calculated using Fiji (ImageJ, U.S. National Institutes of Health, Bethesda, Maryland, USA). Tracking was done using Trackmate, a plugin for automated particle tracking. For imaging at the free end of the tip, automatic tracking was done. For imaging at the truncated end, manual tracking was done. For automatic tracking, 3 videos with 1000 frames each were used. For manual tracking, 3 videos with 500 frames each were used. Microscopic indentations of the tip were used as markers for tracking. Images were cropped to remove noise.

For automatic tracking in Trackmate, the estimated blob diameter of 5–10 pixels was chosen and a threshold of 1–15 was used. The optimum value was chosen for each high-speed video to ensure that one spot as detected for one feature in the image. The simple Linear Assignment Problem (LAP) tracker was used with a linking maximum distance set to 4–7 pixels and a gap closing maximum distance set to 4 pixels. The Trackscheme option was used to link any unlinked spots and delete erroneous spots. The x and y coordinates of the tracked spots in each frame were saved. For manual tracking, spots were manually tracked in Trackmate and the x and y coordinates were saved as before.

3.2. Tip vibration validation

The deformation of the scaler occurs mainly near the free end. The section near the handle is thick and does not deform during vibration. For the case considered, the motion of the scaler is in its symmetric plane, i.e. the *oxy* plane. In our computations we truncate the part that

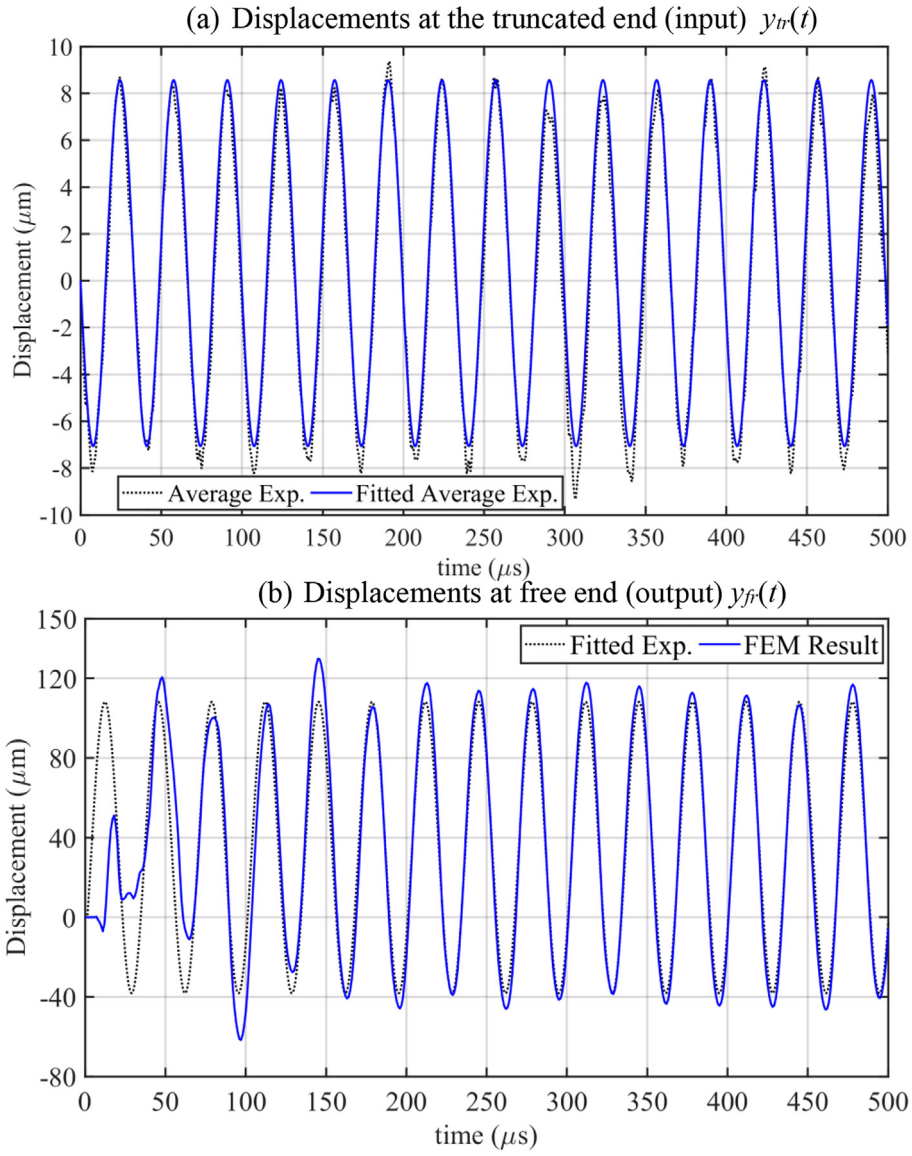

Fig. 4. Comparison between the FEM and the experimentally obtained displacements for ultrasonic dental scaler tip 10P vibrating in water: (a) experimental and smoothed displacements at the truncated end of the scaler along y-axis $y_{tr}(t)$, (b) Displacement at the free end along the y-direction $y_{fr}(t)$. The first term of Fourier series parameters in the calculations were frequency $f = 30$ kHz and $a_0 = 0$ µm, $a_1 = 0$ µm and $b_1 = 8$ µm.

does not deform as shown in Fig. 1a, b, where the deformation is prescribed as a boundary condition. The time histories of the x- and y-coordinates at the truncated end, $x_{tr}(t)$ and $y_{tr}(t)$, were provided from the experiments. To reduce the random and measurement errors, the average values of three experimental recorded displacements were used for the calculation.

However, the averaged data for $x_{tr}(t)$ and $y_{tr}(t)$ are not smooth (dotted black line), as shown in Fig. 4a, due to limitations in the maximum frame rate of the high-speed camera used in this study (900,000 fps). Our calculations showed that the non-smoothed deformation at the truncated end, $x_{tr}(t)$ and $y_{tr}(t)$, resulted in numerical instabilities in the FEM calculations. To resolve this problem, the experimental data were fitted with the first- term of the Fourier series $a_0 + a_1\cos(\omega t) + b_1\sin(\omega t)$, as shown in the Fig. 4a (solid blue line), with $\omega = 2\pi f$, where f is the frequency. This is performed by using a fit function, fit(Data1, Data1, 'fourier1') in MATLAB.

The time history of the displacement at the free end is denoted as $y_{fr}(t)$, since the free end is approximately along the x-axis. Fig. 4b compares the FEM simulation and the experimental data for the displacement at the free end $y_{fr}(t)$. There is a large discrepancy between the results for the first few cycles of oscillation, because the scaler tip and fluid are initially at rest in the computation model but the experimental data were recorded after many cycles. After the first few cycles, the free end displacement $y_{fr}(t)$ rapidly stabilizes and agrees well with the experimental data. The simulation was executed for a period of 1000 µs in all cases throughout this study unless stated otherwise, however only the first 500 µs is presented in Fig. 4 for clarity.

Fig. 5a displays the contours of the pressure in the fluid and the scaler tip displacement along the y-axis (D_y) along the symmetric plane (oxy) at a typical time $t = 256$ µs, for the case in Fig. 4. Fig. 5b shows the corresponding experimental image of the cavitation zone near the straight part of the vibrating scaler tip [18].

The comparison shows that the FEM and experimental results are correlated in terms of the size and location of the cavitation zone as well as the locations of the nodes. The simulated pressure contour (Fig. 5a) shows the predicted areas of cavitation in black. This represents areas where the pressure is 0 Pa, which is the threshold for cavitation. The cavitation zone is close to the tip. This agrees with experimental results where high-speed imaging was used to image the cavitation around the tip [18].

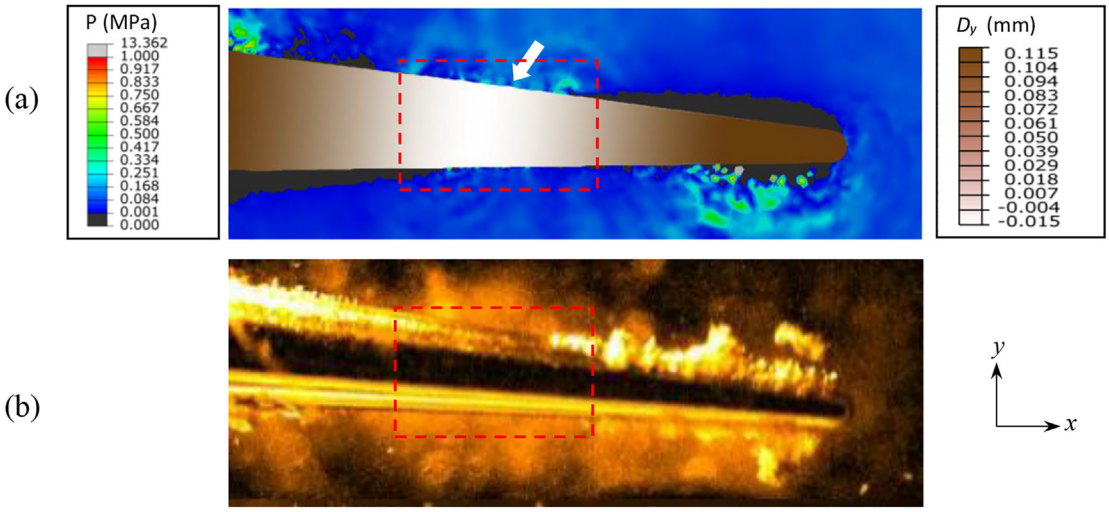

Fig. 5. (a) Contours of the fluid pressure and scaler tip displacement along *y*-axis (D_y) at the symmetric plane (*oxy*) at a typical time $t = 256$ μs for the case in Fig. 4. The black region is considered as the cavitation zone due the pressure reduction to 0 Pa. (b) Experimental high-speed image of cavitation occurring around tip 10P. The tip displacement and cavitation zones are in agreement with the experimental data. The white arrows indicate the point of least displacement. The cavitation volume was calculated based on the summation of the volume of elements which had average pressure values of zero.

The scaler tip displacement is maximum at the free end (red area) and minimum at a location 4–6 mm away from the free end (highlighted by red rectangle) where there is no cavitation. There is a region of cavitation near the free end which is ~3 mm long. This also agrees with experimental results where Felver et al. [17] found that cavitation occurred at the points of maximum tip vibration (antinodes) and no cavitation happened at minimum tip vibration (nodes).

4. Parametric studies using the FEM model

The frequency of ultrasonic dental scalers is fixed in the range of 20–50 kHz [17]. The power of the instrument can be altered, which leads to a change in the amplitude of oscillation. In this section, a parametric study was carried out to investigate the effects of frequency and amplitude on the cavitation occurring.

4.1. Effects of vibration frequency on cavitation

Reconsider the case in Fig. 4 but with various frequencies $f = 22$, 35, 40, 48 and 56 kHz. The volume of cavitation and the root mean square (RMS) amplitude of the tip displacement at the free end are shown in Figs. 6a and 6b, respectively. The total cavitation volume in the whole flow field increases with the frequency. However, the cavitation volume around the straight part of the tip increases with the frequency before 30 kHz, then decreases reaching a minimum at 40 kHz. It then increases again at the free end above 40 kHz. To analyze this trend, we calculated the natural frequency of the scaler vibrating without surrounding liquid with fixing the truncated end using the ABAQUS software, which is 34.7 kHz. Considering the added mass for the scaler vibrating in water, its natural frequency should be decreased.

The RMS amplitude at the free end along the *y*-axis has a maximum at 35 kHz (Fig. 6b) which could be due to the proximity to the natural frequency. On the other hand, although RMS amplitude along *y*-axis at 56 kHz was smaller than the case at 30 kHz, the cavitation volume almost tripled. This could be due to two-dimensional vibration at 56 kHz and unidirectional vibration at 30 kHz, since the RMS amplitude along *x*-axis at 56 kHz was much larger than at 30 kHz. Note that the vibration along the *z*-axis is not considered in this research as it is relatively small $O(10^{-2}–10^{-1})$ μm and it considered as numerical instability.

Fig. 7 shows pressure field in the fluid along the symmetric plane *oxy* at two different time instants at $t = 240$ and 670 μs for the case $f = 56$ kHz. In this case the cavitation zone stretches away from the scaler tip for about ~2–3 mm, unlike the case for $f = 30$ kHz where the cavitation zone mainly attached to the scaler surface (see Fig. 5a). A high pressure zone in the fluid reaching 56 MPa attached to the scaler surface is noteworthy (Fig. 7 Grey color region).

4.2. Effects of vibration amplitude on cavitation

We then consider the effects of the amplitude of oscillation of the scaler for the generation of cavitation. The case in Fig. 4 is re-calculated with various amplitude of oscillation at the truncated end for 7, 9, 10, and 11 μm, respectively. As shown in Fig. 8a, the cavitation volumes in

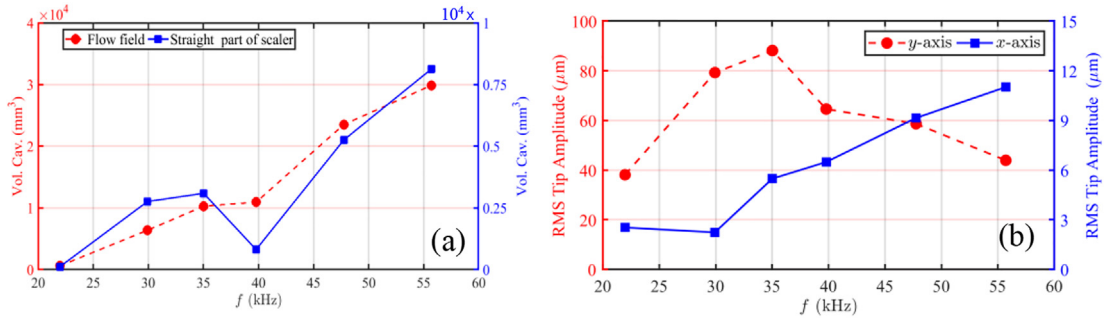

Fig. 6. (a) The volumes of the cavitation zones in the whole flow domain and around straight part of scaler tip, and (b) the RMS amplitude of the scaler tip at the free end along *x* and *y* axis, versus the oscillation frequency of the scaler tip, for the case in Fig. 4.

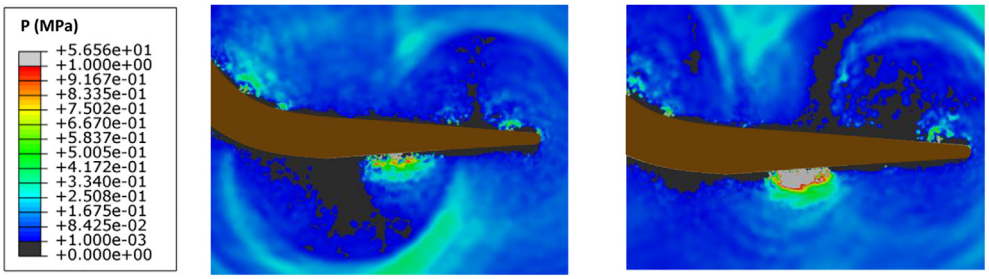

Fig. 7. The pressure counter along symmetric plane *oxy* at frequency 56 kHz at two different time instants $t = 240$ and 670 μs. The remaining parameters are the same as in Fig. 4.

the whole flow field and around the straight part of the scaler tip increase with the amplitude of oscillation, since the scaler oscillating at a large amplitude generates a pressure field oscillating at a large amplitude.

The RMS amplitude of oscillation at the free end along the x and y directions increase linearly with the amplitude of oscillation of the truncated end (Fig. 8b). This correlates with the recent study of Vyas et al. [18] used high-speed imaging which concluded that cavitation around ultrasonic scaler tip and amplitude at the free end increase at higher power settings.

4.3. Effects of wave power on the cavitation

Under the linear approximation, the displacement of a ultrasonic scaler tip can be expressed as a harmonic oscillation: $A\sin(\omega t)$, where A and ω are the amplitude and angular frequency. The average power p_{av} to the fluid from the scaler per unit area per cycle is estimated as

$$p_{av} = \frac{1}{2} c \rho_f \omega^2 A^2 \tag{18}$$

Table 1, shows the cases with the frequency increased and the amplitude decreased to keep p_{av} constant. Subject to the same oscillation power, the cavitation changes significantly with the frequency. The cavitation volume in the whole fluid domain increases with the frequency. However, the cavitation around the straight part of the scaler tip increases with the frequency for $f < 30$ kHz and decreases afterwards, reaching the maximum at $f = 30$ KHz. This trend is consistent to the RMS amplitude at the free end. This is very close to the operation frequency 29 kHz for the scaler.

5. Summary and conclusion

The vibro-acoustic behaviour of a dental ultrasonic scaler tip immersed in water has been numerically modelled using a coupled acoustic-structural finite element code. It is assumed that when the pressure is below the cavitation threshold, the local liquid zone is undergoing cavitation. The finite element predictions of the amplitude oscillation at the free end and the cavitation zone around the scaler tip

Table 1
Cavitation volume in the whole fluid domain and around only the straight part of the scaler tip, and RMS amplitude of the free end at different frequency and amplitude with the average power $p_{av}p_{av*}$ kept constant. The remaining parameters are the same as in Fig. 4.

f (kHz)	A (μm)	Vol. Cav. (mm^3) x10^3		RMS amplitude at free end (μm)	
		Fluid field	Around straight part	y-axis	x-axis
25	9.60	1.51	0.38	63	3
30	8.00	6.37	3.09	79	2
35	6.83	8.89	2.49	76	5
44	5.44	9.26	0.26	43	5

were validated using the experimental data. The parametric studies were performed to investigate the cavitation volume around the scaler tip by changing the frequency and amplitude independently. Based on the numerical results it can be concluded that:

1. As the oscillation frequency of scaler is fixed, the cavitation volume generated increases with the oscillation amplitude.
2. As the amplitude fixed, the cavitation volume in the whole flow field increases with the oscillation frequency, however, the cavitation volume around the straight part of the scaler tip fluctuates with the frequency and has minimum at $f = 40$ kHz.
3. Subject to the same oscillation power, the cavitation volume in the whole fluid domain increases with the frequency. However, the cavitation around the straight part of the scaler tip various significantly with the frequency, reaching the maximum at $f = 30$ KHz.

The results show that modifying the ultrasonic scaler tip vibration by altering the frequency and increasing the vibration amplitude of the tip result in increased cavitation. This may result in increased efficiency of bacterial biofilm removal from the tooth surfaces. In this regard, the numerical model developed in this study can aid in further optimization studies that allow the ultrasonic scaler to be used in a non-contact mode using only the cavitation to clean and creating a novel method of dental

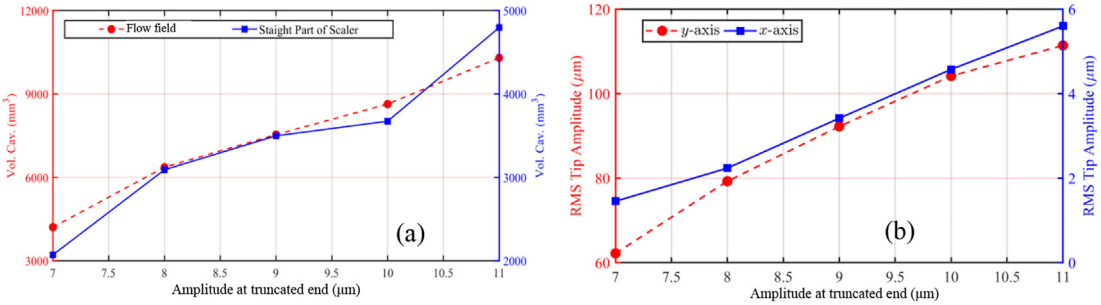

Fig. 8. (a) Cavitation volumes in the whole flow field and around only straight part of the scaler tip, and (b) The RMS amplitude at the free end along × and y directions, versus the amplitude of oscillating of the scaler, for the case in Fig. 4.

implant maintenance.

Acknowledgements

This work was funded by the Engineering and Physical Sciences Research Council (EPSRC) grant number EP/P015743/1.

Appendix A. Supplementary data

Supplementary data to this article can be found online at https://doi.org/10.1016/j.ultsonch.2020.104963.

References:

[1] A.D. Walmsley, W.R. Laird, A.R. Williams, A model system to demonstrate the role of cavitational activity in ultrasonic scaling, J. Dental Res. 63 (1984) 1162–1165.
[2] S.C. Lea, A.D. Walmsley, Mechano-physical and biophysical properties of power-driven scalers: driving the future of powered instrument design and evaluation, Periodontology 51 (2000) 63–78, https://doi.org/10.1111/j.1600-0757.2009.00300.x.
[3] A.D. Walmsley, Ultrasonics in dentistry, Phys. Proc. 63 (2015) 201–207, https://doi.org/10.1016/j.phpro.2015.03.033.
[4] P. Schmage, F. Kahili, I. Nergiz, T.M. Scorziello, U. Platzer, P. Pfeiffer, Cleaning effectiveness of implant prophylaxis instruments, Int. J. Oral Maxillofac. Implants 29 (2) (2014) 331–337, https://doi.org/10.11607/jomi.2524.
[5] Louropoulou, D.E. Slot, F. Van der Weijden, The effects of mechanical instruments on contaminated titanium dental implant surfaces: a systematic review, Clin. Oral Implants Res. 25 (2014) 1149–1160, https://doi.org/10.1111/clr.12224.
[6] T.G. Leighton, The Acoustic Bubble, London Ed., Academic Press, 1994 https://doi.org/10.1017/S0022112094214519.
[7] F.R. Young, Cavitation. World Scientific, 1999. Available at: https://doi.org/10.1142/p172.
[8] K. Yasui, Fundamentals of acoustic cavitation and sonochemistry. In Theoretical and experimental sonochemistry involving inorganic systems, Springer, Dordrecht, 2010, pp. 1–29.
[9] N. Vyas, K. Manmi, Q. Wang, A.J. Jadhav, M. Barigou, R.L. Sammons, S.A. Kuehne, A.D. Walmsley, Which parameters affect biofilm removal with acoustic cavitation? a review, Ultrasound Med. Biol. 45 (5) (2019) 1044–1055, https://doi.org/10.1016/j.ultrasmedbio.2019.01.002.
[10] B. Lozowicka, M. Jankowska, I. Hrynko, P. Kaczynski, Removal of 16 pesticide residues from strawberries by washing with tap and ozone water, ultrasonic cleaning and boiling, Environ. Monit. Assess. 188 (2016) 51, https://doi.org/10.1007/s10661-015-4850-6.
[11] M. Salta, L. Goodes, B. Maas, S. Dennington, T. Secker, T. Leighton, Bubbles versus biofilms: a novel method for the removal of marine biofilms attached on antifouling coatings using an ultrasonically activated water stream, Surf. Topogr. Metrol. Prop. 4 (2016) 034009, , https://doi.org/10.1088/2051-672X/4/3/034009.
[12] R. Fink, M. Oder, E. Strazar, S. Filip, Efficacy of cleaning methods for the removal of Bacillus cereus biofilm from polyurethane conveyor-belts in bakeries, Food Control 80 (2017) 267–272, https://doi.org/10.1016/j.foodcont.2017.05.009.
[13] D.F. Rivas, B. Verhaagen, J.R.T. Seddon, A.G. Zijlstra, L.M. Jiang, L.W.M. Van Der Sluis, M. Versluis, D. Lohse, H.J.G.E. Gardeniers, Localized removal of layers of metal, polymer, or biomaterial by ultrasound cavitation bubbles, Biomicrofluidics 6 (2012) 034114, , https://doi.org/10.1063/1.4747166.
[14] M. Erriu, C. Blus, S. Szmukler-Moncler, S. Buogo, R. Levi, G. Barbato, D. Madonnaripa, G. Denotti, V. Piras, G. Orrù, Microbial biofilm modulation by ultrasound: Current concepts and controversies, Ultrason. Sonochem. 21 (2014) 15–22, https://doi.org/10.1016/j.ultsonch.2013.05.011.
[15] P. Birkin, D. Offin, C. Vian, R. Howlin, J. Dawson, T. Secker, R. Hervé, P. Stoodley, R. Oreffo, C. Keevil, Cold water cleaning of brain proteins, biofilm and bone–harnessing an ultrasonically activated stream, PCCP 17 (2015) 20574–20579.
[16] R. Howlin, S. Fabbri, D. Offin, N. Symonds, K. Kiang, R. Knee, D. Yoganantham, J. Webb, P. Birkin, T. Leighton, Removal of dental biofilms with an ultrasonically activated water stream, J. Dent. Res. 94 (2015) 1303–1309, https://doi.org/10.1039/C5CP02406D.
[17] B. Felver, D.C. King, S.C. Lea, G.J. Price, A.D. Walmsley, Cavitation occurrence around ultrasonic dental scalers, Ultrason. Sonochem. 16 (2009) 692–697, https://doi.org/10.1016/j.ultsonch.2008.11.002.
[18] N. Vyas, E. Pecheva, H. Dehghani, R.L. Sammons, Q.X. Wang, D.M. Leppinen, A.D. Walmsley, High speed imaging of cavitation around dental ultrasonic scaler tips, PLoS One 11 (2016) e0149804, , https://doi.org/10.1371/journal.pone.0149804.
[19] N. Vyas, H. Dehghani, R.L. Sammons, Q.X. Wang, D.M. Leppinen, A.D. Walmsley, Imaging and analysis of individual cavitation microbubbles around dental ultrasonic scalers, Ultrasonics 81 (2017) 66–72, https://doi.org/10.1016/j.ultras.2017.05.015.
[20] W. Lauterborn, T. Kurz, Physics of bubble oscillations, Rep. Prog. Phys. 73 (10) (2010) 106501, , https://doi.org/10.1088/0034-4885/73/10/106501.
[21] W.B. Wu, A.M. Zhang, Y.L. Liu, S.P. Wang, Local discontinuous Galerkin method for far-field underwater explosion shock wave and cavitation, Appl. Ocean Res. 87 (2019) 102–110.
[22] Abaqus. 6.10 User's Documentation, Getting Started with Abaqus Interactive Edition. 2012. Available online: http://dsk.ippt.pan.pl/docs/abaqus/v6.13/books/gsa/default.htm (accessed on 20 January 2018).
[23] J. Park, A Coupled Runge Kutta Discontinuous Galerkin-Direct Ghost Fluid (RKDGDGF) Method To Near-Field Early-Time Underwater Explosion (UNDEX) Simulations, Virginia Polytechnic Institute and State University, USA, 2008.
[24] A.B. Wardlaw, A. Luton, Fluid-structure interaction mechanisms for close-in explosions, Shock Vib. 7 (2007) 265–275.
[25] C.E. Brennen, Chapter 2, Cavitation and Bubble Dynamics, Oxford University Press, 1995.
[26] J.P. Gomes, H. Lienhart, Fluid Structure Interaction II. Modelling, Simulation, Optimization, in: H.-J. Bungartz, M. Mehl, M. Schäfer (Eds.), Lecture Notes in Computational Science and Engineering, Springer, 2010, pp. 383–411 https://doi.org/10.1007/978-3-642-14206-2.
[27] O.C. Zienkiewicz, R.L. Taylor, P. Nithiarasu, The Finite Element Method for Fluid Dynamics (Seventh Edition) 2014.https://doi.org/10.1016/b978-1-85617-635-4.00016-9.
[28] T. He, K. Zhang, An overview of the combined interface boundary condition method for fluid–structure interaction, Arch. Comput. Methods Eng. 24 (4) (2017) 891–934, https://doi.org/10.1007/s11831-016-9193-0.
[29] Z. Aman, Z. Weixing, W. Shiping, F. Linhan, Dynamic response of the non-contact underwater explosions on naval equipment, Mar. Struct. 24 (4) (2011) 396–411, https://doi.org/10.1016/j.marstruc.2011.05.005.
[30] T. Łodygowski, W. Sumelka, Limitations in application of finite element method in acoustic numerical simulation, J. Theor. Appl. Mech. 44 (2006) 849–865.
[31] M. Abdullahi, S. Oyadiji, Acoustic wave propagation in air-filled pipes using finite element analysis, Appl. Sci. 8 (8) (2018) 1318, https://doi.org/10.3390/app8081318.
[32] H. Zhou, T. Liu, R. Guo, R. Liu, P. Song, Numerical investigation on water blast response of freestanding carbon fiber reinforced composite sandwich plates with square honeycomb cores, Appl. Compos. Mater. 26 (2) (2018) 605–625, https://doi.org/10.1007/s10443-018-9737-6.
[33] A.J. Moradloo, A. Adib, A. Pirooznia, Damage analysis of arch concrete dams subjected to the underwater explosion, Appl. Math. Model. (2019) (in press).
[34] S.C. Trenter, A.D. Walmsley, G. Landini, J.M. Shippen, Assessment of the ultrasonic dental scaler insert, Med. Eng. Phys. 24 (2002) 139–144, https://doi.org/10.1016/s1350-4533(01)00103-5.